Dynamical spin susceptibility of a spin-valley half-metal

D. A. Khokhlov,[1,2,3] A. L. Rakhmanov,[1,2,4] A. V. Rozhkov,[2,4,5] and A. O. Sboychakov[4]

[1]*Dukhov Research Institute of Automatics (VNIIA), 127055 Moscow, Russia*
[2]*Moscow Institute of Physics and Technology, Institutsky Lane 9, Dolgoprudny, Moscow region, 141700, Russia*
[3]*National Research University Higher School of Economics, Moscow 101000, Russia*
[4]*Institute for Theoretical and Applied Electrodynamics, Russian Academy of Sciences, Moscow 125412, Russia*
[5]*Skolkovo Institute of Science and Technology, Skolkovo Innovation Center 3, Moscow 143026, Russia*

(Received 17 February 2020; revised manuscript received 24 April 2020; accepted 3 June 2020; published 18 June 2020)

A few years ago we predicted theoretically that in systems with nesting of the Fermi surface the spin-valley half-metal has lower energy than the spin density wave state. In this paper we suggest a possible way to distinguish these phases experimentally. We calculate the dynamical spin susceptibility tensor for both states in the framework of the Kubo formalism. Discussed phases have different numbers of bands: four bands in the spin-valley half-metal and only two bands in the spin density wave. Therefore, their susceptibilities, as functions of frequency, have different numbers of peaks. Besides, the spin-valley half-metal does not have rotational symmetry, thus, in general the off-diagonal components of the susceptibility tensor are nonzero. The spin density wave obeys robust rotational symmetry and off-diagonal components of the susceptibility tensor are zero. These characteristic features can be observed in experiments with inelastic neutron scattering.

DOI: 10.1103/PhysRevB.101.235141

I. INTRODUCTION

The concept of Fermi surface nesting plays an important role in the studies of systems with more than one electronic band [1–24]. In the presence of nesting electronic liquid becomes unstable and an ordered state emerges. The ordered phases associated with the nesting are commensurate and incommensurate spin density wave [1] (SDW), charge density wave [25], inhomogeneous antiferromagnetism [2], as well as others. Recently we argued that a half-metallic and the so-called spin-valley half-metal (SVHM) may be stabilized in a system with nesting [9,11]. Half-metals [26–28] are well known for several decades. This class of metals is characterized by perfect spin polarization of the charge carriers on the Fermi surface. Consequently, electric current in a half-metal carries not only charge but spin as well. The latter property is of interest for applications in spintronics. By the same token, the electronic states at the Fermi surface of the spin-valley half-metal are perfectly polarized with respect to the so-called spin-valley index. Thus, the SVHM can conduct a spin-valley polarized current. The spin-valley polarized currents are of interest for applications [29]. In addition, the SVHM state does not require strong electron-electron interaction for its stability. Consequently, the SVHM can be realized without transition metals in its chemical composition, which makes such materials applicable in biocompatible devices.

Theoretically, the SVHM state was identified in a model with perfect nesting and weak electron-electron interaction. When the perfect nesting is partially destroyed by doping, parental insulating SDW is replaced by the SVHM phase [3]: Calculations within the framework of such a minimal model show that the SVHM phase has lower free energy than the SDW and the paramagnetic phase, at least, for low temperatures [3]. Depending on details, the SVHM may be either commensurate or incommensurate [3,9]. It competes against several related phases, such as (i) commensurate SDW, (ii) incommensurate SDW, (iii) inhomogeneous SDW.

As shown in Refs. [3,9], the SVHM has a number of distinctive features which separate it from phases (i)–(iii). For example, magnetic structure of the SVHM state possesses a magnetic helical component, which superimposes on the purely collinear SDW order. Besides this, the symmetry between single-electron states with different spin-valley index is preserved in the ordered states (i)–(iii) but is lifted in the SVHM. As a result, the number of nondegenerate single-electron bands in the SVHM is two times bigger than in the SDW.

It follows from our previous studies that the search for materials realizing the SVHM state should be limited to the electronic systems that demonstrate the nesting-driven SDW sensitive to doping. There are several classes of materials satisfying this requirement: chromium and its alloys [30–33], some topological insulators [34], iron-based materials [35], as well as other systems [36–38].

However, the SVHM has not been observed experimentally yet. In this paper, we discuss a possibility of detecting the SVHM phase using inelastic neutron scattering. For many materials, neutron scattering has been successfully applied to investigate their magnetic and superconducting properties. Comparing observed spectrum with a theoretical prediction, useful pieces of information can be obtained [25,39–48]. It is natural to expect that such an experimental tool can play an important role in search for the SVHM order.

Below we propose a method to discriminate between the SVHM and the SDW phases. It relies on the fact that the SVHM has at least four nondegenerate bands close to the

Fermi level, whereas the SDW has two doubly degenerate bands. Consequently, in these thermodynamic phases, the electronic contributions to the neutron cross section are nonidentical, and phase-specific features in the neutron spectrum can be used for identification of an ordered state in a candidate material.

Technically, the electronic contribution to the neutron cross section is described by the dynamical spin susceptibility tensor. Using Kubo formalism within the framework of the minimal model of Refs. [3,9] we determine this tensor for the commensurate SVHM and SDW phases. Our calculations demonstrate that the neutron scattering spectrum of the SVHM has three high-intensity peaks, in contrast to the SDW, whose spectrum has only one pronounced peak. We also discuss other features of the spin susceptibility tensor. The presented derivation does not aim at a specific material, instead, the obtained results demonstrate general features and peculiarities of the neutron scattering on an SVHM material, which may be used to identify the SVHM phase.

This paper is organized as follows. In Sec. II we briefly describe the two band model used in calculations. In Secs. III and IV we calculate the susceptibility tensor for the SDW and the SVHM, respectively. Summary and conclusions are in Sec. V.

II. MODEL

A. SVHM and SDW phases

We start with the outline of the basic structure of the minimal model [3] which hosts the SVHM as one of its possible ground states. The model Hamiltonian has two single-electron bands, or valleys, which are referred to as a and b. If we neglect the electron-electron repulsion, their band dispersions are assumed to be parabolic [Fig. 1(a)]

$$\epsilon_a(\mathbf{k}) = \frac{k^2 - k_F^2}{2m_a} - \mu = \xi_k^a - \mu,$$
$$\epsilon_b(\mathbf{k}+\mathbf{Q}_0) = \frac{-k^2 + k_F^2}{2m_b} - \mu = -\xi_k^b - \mu. \quad (1)$$

We use a system of units, where $\hbar = 1$. Here μ is the chemical potential. When $\mu = 0$, the Fermi surface of the valley a, after translation by the nesting vector $\mathbf{Q}_0$, exactly matches the Fermi surface of the valley b. Such a property of the band structure is called a perfect nesting. It is convenient to measure doping relative to the $\mu = 0$ state treating the latter state as undoped. Momentum $k_F = \sqrt{2m\epsilon_F}$ is a radius of the Fermi sphere for both the a and b valleys at the perfect nesting. In addition, we introduce the Fermi velocity $v_F = k_F/m$. Unless the opposite is stated, we assume that effective masses m_a and m_b are equal to each other. In such a case, the subscript may be dropped, both masses can be denoted by symbol m, and $\xi_k^a = \xi_k^b = \xi_k$. Each band has a density of states $N_F = mk_F/(2\pi^2)$ at the Fermi level.

Next, we take into account a weak electron-electron repulsion, which we assume to be short range. The part of the interaction which is responsible for the magnetic ordering is:

$$H_{\text{int}} = \frac{g}{V}\sum_{\mathbf{k}\mathbf{k}'\sigma} a^\dagger_{\sigma\mathbf{k}} a_{\sigma\mathbf{k}} b^\dagger_{\overline{\sigma}\mathbf{k}'} b_{\overline{\sigma}\mathbf{k}'}, \quad (2)$$

where operator $a_{\sigma\mathbf{k}}$ (operator $b_{\sigma\mathbf{k}}$) represents annihilation operator of an electron with the spin σ in the valley a (valley b) at the wave vector $\mathbf{k}$. For the operators $a_{\sigma\mathbf{k}}$ and $b_{\sigma\mathbf{k}}$, the wave vector $\mathbf{k}$ is measured from the center of the corresponding valley. Notation $\overline{\sigma}$ means $-\sigma$. The interaction constant g is assumed to be small: $gN_F \ll 1$. We simplify the Hamiltonian via mean field approach. There are two order parameters labeled by $\sigma = \pm 1$

$$\Delta_\sigma = \frac{g}{V}\sum_{\mathbf{k}} \langle a^\dagger_{\sigma\mathbf{k}} b_{\overline{\sigma}\mathbf{k}}\rangle, \quad (3)$$

where V is the volume of the system.

Now we can write down the full mean field Hamiltonian

$$H = \sum_{\mathbf{k}\sigma}\big[(\xi_\mathbf{k} - \mu)a^\dagger_{\sigma\mathbf{k}} a_{\sigma\mathbf{k}} + (-\xi_\mathbf{k} - \mu) b^\dagger_{\sigma\mathbf{k}} b_{\sigma\mathbf{k}} - \Delta_\sigma b^\dagger_{\overline{\sigma}\mathbf{k}} a_{\sigma\mathbf{k}} - \Delta_{\overline{\sigma}} a^\dagger_{\sigma\mathbf{k}} b_{\overline{\sigma}\mathbf{k}}\big] + \frac{V}{g}\big(\Delta_\uparrow^2 + \Delta_\downarrow^2\big). \quad (4)$$

To diagonalize the Hamiltonian (4) we perform the Bogolyubov transformation. The obtained quasiparticle spectrum consists of four bands:

$$E^{(s)}_{\sigma\mathbf{k}} = \pm\sqrt{\xi_k^2 + \Delta_\sigma^2}, \quad (5)$$

where each band is labeled by two indexes: σ and $s = 1, 2$. Here $s = 1$ corresponds to sign "$-$" and $s = 2$ to sign "$+$."

To obtain Δ_σ we should minimize the total energy of the system. After the minimization at zero doping one may see that the order parameters does not depend on the index σ, thus, the quasiparticle bands are double degenerate. Consequently, $\mu = 0$ state possesses SDW order with static spin polarization

$$\langle S_x(\mathbf{r})\rangle = \frac{\Delta_\sigma + \Delta_{\overline{\sigma}}}{g}\cos(\mathbf{r}\mathbf{Q}_0),\ \langle S_y(\mathbf{r})\rangle = \langle S_z(\mathbf{r})\rangle = 0. \quad (6)$$

Band structure of the SDW is schematically shown in Fig. 1(b).

Now let us study the effect of the doping on the SDW state. In many papers [1,2,12] the energy minimization was performed under the following constraint

$$\Delta_\sigma = \Delta_{\overline{\sigma}} = \Delta. \quad (7)$$

Minimizing the total energy under the condition (7) we find Δ as a function of doping. The resultant state is the SDW metal [1,2]. Quasiparticle bands at nonzero doping are shown in Fig. 1(c). They remain doubly degenerate, since we employ restriction (7).

However, in a more general case the condition (7) can be discarded. Instead, the total energy is minimized as a function of two variables Δ_σ and $\Delta_{\overline{\sigma}}$. The latter minimization is simplified by the fact that the mean field Hamiltonian (4) split into a sum of two decoupled terms, each describing a particular sector of single-particle states. The first term represents (i) electrons from the valley a with the spin σ and (ii) electrons from the valley b with the spin $\overline{\sigma}$. These quasiparticle states form sector σ. The order in sector σ is characterized by Δ_σ. The second term of the mean field Hamiltonian represents electrons from the valley a with spin $\overline{\sigma}$ and from the valley b with spin σ. Such states constitute sector $\overline{\sigma}$. Parameter $\Delta_{\overline{\sigma}}$ describes order in sector $\overline{\sigma}$.

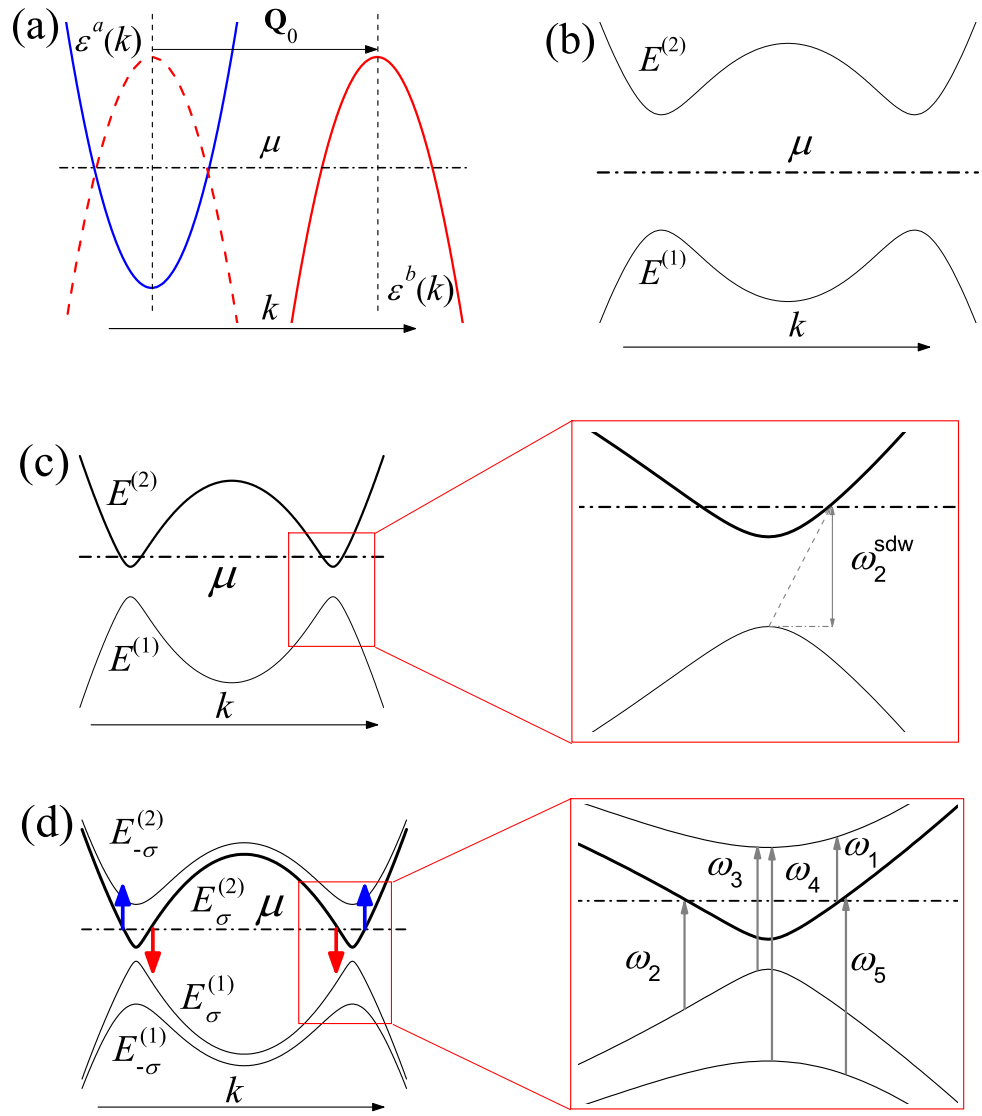

FIG. 1. The energy of single-electron and quasiparticle bands (vertical axis) versus momentum (horizontal axis) for different order parameters and doping values. (a) Bare single-particle bands. The (blue) solid line represents the electron dispersion (band a); the (red) solid line is the hole dispersion (band b). The translated hole band is shown by dashed line. Arrow $\mathbf{Q}_0$ corresponds to the nesting vector. The dashed-dotted horizontal line is the Fermi energy of the undoped state, when the nesting is perfect. (b)–(d) Band structure when the effects of weak electron-electron repulsion are taken into account. (b) The band structure of the undoped SDW state. The chemical potential level (dash-dotted line) lies in the spectral gap separating filled band $E^{(1)}$ and empty band $E^{(2)}$. Both bands are doubly degenerate. (c) The band structure of the doped SDW state. The bands are shown by solid lines. The chemical potential crosses the upper band $E^{(2)}$ which becomes partially filled. The vertical arrow in the insets indicates quasiparticle interband transition at the threshold frequency ω_2^{sdw}, see Eq. (29). (d) The quasiparticle band structure of the SVHM phase. Double degeneracy present in the SDW state is lifted, and all four bands are distinct. The Fermi surface is polarized with respect to the spin-valley index. Up and down bold arrows illustrate this polarization. Up arrows (blue) show spin-up electrons from the valley a, down arrows (red) show spin-down electrons from the valley b. The vertical arrows in the inset illustrate minimum energies which are required to open a specific interband scattering channel. The frequencies $\omega_1, \ldots, \omega_5$ are defined by Eq. (32).

Doping is not required to distribute equally between the sectors [3,12]. To demonstrate this, let us write the following expression for the grand potential Ω

$$\Omega = \Omega_\sigma + \Omega_{\bar\sigma} = \frac{V}{g}\left(\Delta_\sigma^2 + \Delta_{\bar\sigma}^2\right) - \sum_{\mathbf{k}\sigma}\left[\mu - E^{(1)}_{\sigma\mathbf{k}} + \left(\mu - E^{(2)}_{\sigma\mathbf{k}}\right)\theta\left(\mu - E^{(2)}_{\sigma\mathbf{k}}\right)\right], \quad (8)$$

where $\theta(\cdot)$ is the Heaviside step function which replaces Fermi distribution function at zero temperature. In this equation the grand potential Ω is expressed as a sum of partial grand potentials Ω_σ, each representing a specific sector.

It is convenient to introduce partial doping concentrations $x_\sigma = -(1/V)\partial\Omega_\sigma/\partial\mu$. The sum of two partial concentrations equals to total doping concentration

$$x = x_\sigma + x_{\bar\sigma}. \quad (9)$$

Minimization of Ω produces two equations for each σ

$$\frac{\partial\Omega_\sigma}{\partial\Delta_\sigma}=0,\quad \frac{\partial\Omega_\sigma}{\partial\mu}=-x_\sigma V. \tag{10}$$

They must be solved under constraint (9). The system of equations (10) has two types of formal solutions. First type can be found at finite partial doping $x_\sigma > 0$:

$$\Delta_\sigma=\Delta_0\sqrt{1-\frac{x_\sigma}{N_F\Delta_0}}, \tag{11}$$

$$\mu=\Delta_0-\frac{x_\sigma}{2N_F}, \tag{12}$$

where Δ_0 is the order parameter at zero doping in the SDW phase. Similar expressions are derived for negative x_σ. The second solution is, in some sense, "trivial:" if

$$-\Delta_0<\mu<\Delta_0, \tag{13}$$

then

$$\Delta_\sigma=\Delta_0,\quad x_\sigma\equiv 0. \tag{14}$$

That is, for any μ within the gap, sector σ remains undoped, with the order parameter equal to Δ_0.

If solution (14) is overlooked, the only possibility to satisfy Eq. (12) and the constraint (9) is to demand that $x_\sigma = x_{\bar\sigma} = x/2$. In such a case, Eq. (7) is recovered, with $\Delta = \Delta_0\sqrt{1-x/(2N_F\Delta_0)}$. The mean field ground state described by these relations possesses obvious symmetry between the sectors.

However, a many-electron state violating the latter symmetry also exists: One can apply Eqs. (11) and (12) to sector σ and Eq. (14) to sector $\bar\sigma$. For this to be consistent with Eq. (9), we need to assign $x_\sigma = x, x_{\bar\sigma} = 0$. Consequently

$$\Delta_\sigma=\Delta_0\sqrt{1-\frac{x}{N_F\Delta_0}},\quad \Delta_{\overline\sigma}=\Delta_0 \tag{15}$$

for not too strong doping. Using Eq. (12), one further derives $\mu = \Delta_0 - x/(2N_F)$, which also satisfies the inequality (13).

The symmetric state, Eq. (7), corresponds to the doped SDW case. It was discussed in the theoretical literature for several decades. Yet, it is straightforward to demonstrate (for details, consult Refs. [3,9]) that the SVHM phase represented by Eq. (15) has lower free energy. In other words, within the framework of the chosen model the SVHM state is more stable than the SDW.

In contrast with the SDW phase, where $\Delta_\sigma = \Delta_{\overline\sigma}$, the SVHM has two nonzero spin projections:

$$\langle S_x(\mathbf{r})\rangle=\frac{\Delta_\sigma+\Delta_{\overline\sigma}}{g}\cos(\mathbf{r}\mathbf{Q}_0),$$

$$\langle S_y(\mathbf{r})\rangle=\frac{\Delta_\sigma-\Delta_{\overline\sigma}}{g}\sin(\mathbf{r}\mathbf{Q}_0). \tag{16}$$

Since order parameters (15) are unequal to each other, four bands which are defined in Eq. (5) are no longer degenerate, and the Fermi surface appears. We may define [3] the spin-valley index S_v as follows

$$S_v=1 \leftrightarrow \text{electronic states from sector } \sigma,$$

$$S_v=-1 \leftrightarrow \text{electronic states from sector } \overline\sigma. \tag{17}$$

The Fermi surface states are polarized in the spin-valley space, see Fig. 1(d). This fact can be trivially verified since the partially filled band is composed entirely from the electronic states belonging to sector σ. Following Ref. [3], we call this phase the spin-valley half-metal.

B. The dynamical spin susceptibility tensor

Here we discuss the dynamical spin susceptibility tensor in the context of our problem. The Fourier components of the spin projection on the β axis is:

$$S^{\rm s}_\beta(\mathbf{q},t)=\sum_{\mathbf{k}\mu\nu}\sigma^\beta_{\mu\nu}\left[a^\dagger_{\mu\mathbf{k}+\mathbf{q}}(t)\,a_{\nu\mathbf{k}}(t)+b^\dagger_{\mu\mathbf{k}+\mathbf{q}}(t)\,b_{\nu\mathbf{k}}(t)\right],$$

$$S^{\rm f}_\beta(\mathbf{q}+\mathbf{Q}_0,t)=\sum_{\mathbf{k}\mu\nu}\sigma^\beta_{\mu\nu}a^\dagger_{\mu\mathbf{k}+\mathbf{q}}(t)b_{\nu\mathbf{k}}(t)\,,$$

$$S^{\rm f}_\beta(\mathbf{q}-\mathbf{Q}_0,t)=\sum_{\mathbf{k}\mu\nu}\sigma^\beta_{\mu\nu}b^\dagger_{\mu\mathbf{k}+\mathbf{q}}(t)a_{\nu\mathbf{k}}(t)\,. \tag{18}$$

Here $\sigma^\beta_{\mu\nu}$ is (μ,ν) matrix element of a Pauli matrix and $\beta = x, y$ or z. The superscript 's' (superscript 'f') stands for 'slow' ('fast'). The slow term $S^{\rm s}_\beta(\mathbf{q},t)$ oscillates in the real space with the wave vector $\mathbf{q}$, which we restrict to be in the range of $q \lesssim \Delta_0/v_F \ll k_F \sim |\mathbf{Q}_0|$, where $q = |\mathbf{q}|$. This term contains only products of operators from one valley. In other words, it is diagonal in valley index. The fast terms $S^{\rm f}_\beta(\mathbf{q}\pm\mathbf{Q}_0,t)$ oscillate in the real space with the wave vectors $\mathbf{q}\pm\mathbf{Q}_0$. Unlike $S^{\rm s}$, operators $S^{\rm f}$ mix states from different valleys. Indeed, as one can see from their definition, each $S^{\rm f}$ is a sum of terms that themselves are products of two single-electron operators, one single-electron operator is from valley a and another one is from valley b.

The susceptibility is defined in the Kubo formalism [49]

$$\chi^{\rm s(f)}_{\alpha\beta}(\mathbf{Q},\omega)=i\int_0^\infty\left\langle\left[S^{\rm s(f)}_\alpha(\mathbf{Q},t);S^{\rm s(f)}_\beta(-\mathbf{Q},0)\right]\right\rangle e^{i\omega t}dt, \tag{19}$$

where $[A;B] = AB - BA$. Symbol $\langle\ldots\rangle$ denotes averaging with respect to a ground state of a studied phase. We assume that $\mathbf{Q} = \mathbf{q}$ for the slow term and $\mathbf{Q} = \mathbf{q}\pm\mathbf{Q}_0$ for the fast terms. Besides $\chi^{\rm s(f)}_{\alpha\beta}$ defined by Eq. (19), it is possible to introduce the cross terms, describing correlation functions between slow and fast spin densities $\chi^{\rm sf} \sim \langle S^{\rm s}S^{\rm f}\rangle$. However, these quantities do not contribute to the neutron cross section, and we do not consider them.

Further, as we want to describe neutron scattering, we focus only on the part of the tensor which corresponds to the energy conservation law

$$\tilde\chi^{\rm s(f)}_{\alpha\beta}(\mathbf{Q},\omega)=i\int_{-\infty}^\infty\left\langle\left[S^{\rm s(f)}_\alpha(\mathbf{Q},t);S^{\rm s(f)}_\beta(-\mathbf{Q},0)\right]\right\rangle e^{i\omega t}dt. \tag{20}$$

Here integration over all real t gives Dirac δ function which ensures energy conservation in the scattering processes. Related result in a less general case was discussed in Ref. [50] [see Eq. (2.46) in section 2.6 for more details]. In our numerical calculation, the Dirac δ function is approximated by a rectangular function. This function equals to $10^3\Delta_0^{-1}$ over finite support, whose width is $10^{-3}\Delta_0$ (as required by the definition of the Dirac function, the area under our rectangular function is equal to unity).

Direct calculations show that all diagonal components $\tilde{\chi}^{\mathrm{f,s}}_{\alpha\alpha}$ and off-diagonal components $\tilde{\chi}^{\mathrm{f,s}}_{xy,yx}$ may be nonzero. All other components of the dynamical susceptibility vanish within the framework of the discussed model. To calculate $\tilde{\chi}^{\mathrm{f,s}}_{\alpha\beta}(\mathbf{Q},\omega)$ we substitute Eq. (18) into formula (20) and apply the Wick theorem with respect to the studied state. The results of these calculations are presented below.

III. SPIN SUSCEPTIBILITY OF THE SDW PHASE

A. Structure of the susceptibility tensor in the SDW phase

We would like to start with several general statements about the susceptibility tensor of the SDW phase. In the commensurate SDW state the slow term $\tilde{\chi}^{\mathrm{s}}_{\alpha\beta}(\mathbf{Q},\omega)$ of the susceptibility tensor does not depend on direction of the wave vector $\mathbf{Q}=\mathbf{q}$, and the fast term $\tilde{\chi}^{\mathrm{f}}_{\alpha\beta}(\mathbf{Q},\omega)$ of the tensor does not depend on the direction of the vector $\mathbf{Q}-\mathbf{Q}_0=\mathbf{q}$. The same property holds true in the commensurate SVHM phase discussed in Sec. IV. Obviously, this circumstance significantly simplifies the presentation and analysis of our results.

Since the average local spin in the SDW is directed along the x axis, the magnetic structure of the phase possesses a rotational symmetry around the x axis. Therefore, we obtain

$$\tilde{\chi}^{\mathrm{s}}_{\perp}(\mathbf{q},\omega)=\tilde{\chi}^{\mathrm{s}}_{yy}(\mathbf{q},\omega)=\tilde{\chi}^{\mathrm{s}}_{zz}(\mathbf{q},\omega)\neq\tilde{\chi}^{\mathrm{s}}_{xx}(\mathbf{q},\omega), \tag{21}$$

where symbol $\tilde{\chi}^{\mathrm{s}}_{\perp}$ is defined as $\tilde{\chi}^{\mathrm{s}}_{\perp}=\tilde{\chi}^{\mathrm{s}}_{zz,yy}$. Susceptibility $\tilde{\chi}^{\mathrm{f}}_{\perp}$ is defined similarly.

As for the off-diagonal components, $\tilde{\chi}^{\mathrm{s,f}}_{xz}$ and $\tilde{\chi}^{\mathrm{s,f}}_{yz}$ vanish, as discussed in Sec. II B. The presence of the rotational symmetry with respect to the x axis implies nullification of other off-diagonal components as well. Indeed, any rotation around the x axis preserves the susceptibility tensor. At the same time, after rotation on angle equal to π, components $\tilde{\chi}^{\mathrm{s,f}}_{xy,yx}(\mathbf{Q},\omega)$ must change sign. Therefore, we conclude that

$$\tilde{\chi}^{\mathrm{s,f}}_{xy}(\mathbf{Q},\omega)=\tilde{\chi}^{\mathrm{s,f}}_{yx}(\mathbf{Q},\omega)=0. \tag{22}$$

Since relations (21) and (22) are conditioned by the rotational symmetry of the SDW order parameter, they remain valid even when $m_a\neq m_b$. In other words, asymmetry between the electrons and holes does not destroy (21) and (22) in the SDW phase.

Diagonal components of the fast part of the susceptibility tensor obey yet another relation

$$\tilde{\chi}^{\mathrm{f}}_{\perp}(\mathbf{q}\pm\mathbf{Q}_0,\omega)=\tilde{\chi}^{\mathrm{f}}_{xx}(\mathbf{q}\pm\mathbf{Q}_0,\omega). \tag{23}$$

It can be derived by substituting Eq. (18) into Eq. (20). [Let us remark that Eqs. (21) and (22) can be derived by the same substitution as well, without use of symmetry.]

B. Evaluation of the susceptibility tensor

The above analysis demonstrates that, to characterize the neutron scattering by electronic subsystem in the SDW state, one needs to know $\tilde{\chi}^{\mathrm{s,f}}_{\perp}(\mathbf{Q},\omega)$ and $\tilde{\chi}^{\mathrm{s,f}}_{xx}(\mathbf{Q},\omega)$. We determine these quantities numerically using Eq. (20). To be specific, our calculation in the SDW and SVHM phases are performed at

$$x=0.75N_F\Delta_0. \tag{24}$$

For such a doping level, parameters Δ and Δ_σ deviate significantly from Δ_0. Specifically, in the SDW phase, the order parameter and the chemical potential are [2]

$$\Delta\approx 0.79\Delta_0,\quad \mu\approx 0.81\Delta_0. \tag{25}$$

We plot $\tilde{\chi}^{\mathrm{s,f}}(\mathbf{Q},\omega)$ as a function of the energy ω at the fixed wave vector $\mathbf{Q}$, see Fig. 2. Features that are of interest to us are most discernible when $q\lesssim\Delta_0/v_F$. We present $\tilde{\chi}_{\perp}(\mathbf{Q},\omega)$ and $\tilde{\chi}_{xx}(\mathbf{Q},\omega)$ for $q=0.1\Delta_0/v_F$ in Figs. 2(a) and 2(b) and for $q=0.75\Delta_0/v_F$ in Figs. 2(c) and 2(d), respectively.

Each component of the susceptibility tensor in Fig. 2 has a peak at low frequency. It corresponds to electron-hole pairs in the conduction band which are excited by neutrons. These peaks are localized between $\omega=0$ and a threshold frequency ω_1^{sdw}. To derive ω_1^{sdw} we write the energy conservation law for the intraband transitions

$$E^{(2)}_{\mathbf{k}+\mathbf{q}}-E^{(2)}_{\mathbf{k}}=\omega. \tag{26}$$

This must be solved together with

$$\theta\big(\mu-E^{(2)}_{\mathbf{k}}\big)\theta\big(E^{(2)}_{\mathbf{k}+\mathbf{q}}-\mu\big)=1, \tag{27}$$

which is a consequence of Fermi-Dirac statistics. System of equations (26) and (27) for the unknown variable $\mathbf{k}$ has solutions only when $0<\omega<\omega_1^{\mathrm{sdw}}$, where

$$\omega_1^{\mathrm{sdw}}=\sqrt{(\sqrt{\mu^2-\Delta^2}+q)^2+\Delta^2}-\mu. \tag{28}$$

Substituting specific values of q, one finds that $\omega_1^{\mathrm{sdw}}\approx 0.4\Delta_0$ when $q=0.75\Delta_0/v_F$, and $\omega_1^{\mathrm{sdw}}\approx 0.03\Delta_0$ when $q=0.1\Delta_0/v_F$. Both values for ω_1^{sdw} are perfectly consistent with the numerical curves shown in Fig. 2.

Another characteristic frequency ω_2^{sdw} in Fig. 2 is the threshold energy for the inelastic interband electron scattering, see inset in Fig. 1(c). When ω exceeds ω_2^{sdw}, a new scattering channel opens, and the susceptibility becomes finite. This is clearly visible on all panels of Fig. 2.

To evaluate ω_2^{sdw}, similar to our derivation of Eq. (28), we use energy and momentum conservation laws and Fermi-Dirac statistics of electrons to obtain

$$\omega_2^{\mathrm{sdw}}=\Delta+\mu\approx 1.6\Delta_0. \tag{29}$$

This equation has simple interpretation: It is exactly the energy necessary to promote a quasiparticle from a state at the maximum of the completely filled valence band to an empty state at the chemical potential level in the partially filled conductance band. For chosen values of Δ, μ, and q, such a transition is indeed consistent with both energy and momentum conservation laws.

One can notice that for $\omega>\omega_2^{\mathrm{sdw}}$ the susceptibility tensor components pass through a maximum near ω_2^{sdw}. Locations of these peaks are slightly shifted to higher frequencies with respect to ω_2^{sdw}. This 'blueshift,' as well as a nonmonotonic behavior of susceptibility, occurs due to the structure of the joint density of states

$$\rho^{ss'}_{\sigma\sigma'}(\mathbf{q},\omega)=\int\delta(E^{(s)}_{\sigma\mathbf{k}}-E^{(s')}_{\sigma'\mathbf{k}+\mathbf{q}}-\omega)\frac{d^3\mathbf{k}}{(2\pi)^3}. \tag{30}$$

We see in Fig. 2(d) that $\tilde{\chi}^{\mathrm{s}}_{xx}(\mathbf{Q},\omega)$, as a function of $(\omega-\omega_2^{\mathrm{sdw}})$, demonstrates slower (linear) growth than $\tilde{\chi}^{\mathrm{f}}_{xx}(\mathbf{Q},\omega)$. This is a consequence of nullification of the matrix element for

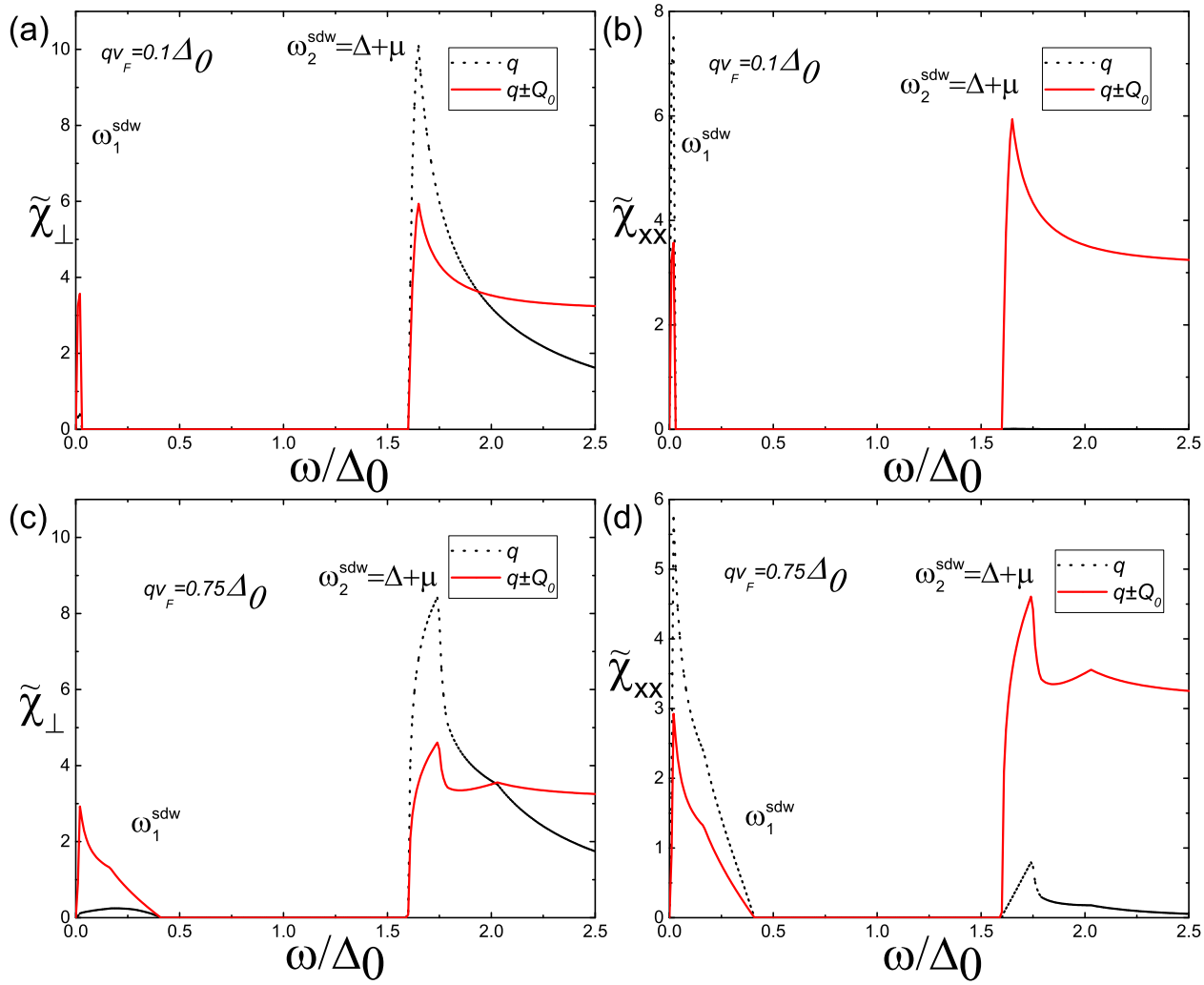

FIG. 2. The diagonal components of the susceptibility tensor $\tilde{\chi}^{s,f}_{\alpha\beta}(\mathbf{Q},\omega)$ at fixed momentum $\mathbf{Q}$ versus frequency ω in the SDW phase. Dot curves show the slow part of the susceptibility calculated for $\mathbf{Q}=\mathbf{q}$; solid curves show the fast part of the susceptibility calculated for $\mathbf{Q}=\mathbf{q}\pm\mathbf{Q}_0$. Panels (a) and (c) present $\tilde{\chi}_\perp(\mathbf{Q},\omega)$, panels (b) and (d) present $\tilde{\chi}_{xx}(\mathbf{Q},\omega)$. The data in panels (a) and (b) is plotted for $q=0.1\Delta_0/v_F$. The data in panels (c) and (d) is plotted for $q=0.75\Delta_0/v_F$. Peaks at low frequency exist due to intraband electron transitions in the conduction band. They start from $\omega=0$ and disappear beyond ω_1^{sdw} [the latter frequency is defined in Eq. (28)]. Peaks close to ω_2^{sdw} arise due to electron transitions from the valence band to the conduction band shown in the inset in Fig. 1(c). The frequency ω_2^{sdw} is the threshold frequency for this process. This energy is defined in Eq. (29).

the corresponding interband electron transition exactly at $\omega=\omega_2^{sdw}$. The matrix element becomes nonzero when $\omega>\omega_2^{sdw}$, however, its value remains small for small q. Thus, $\tilde{\chi}^s_{xx}(\mathbf{Q},\omega)$ in Fig. 2(b) is very close to zero in contrast with $\tilde{\chi}^s_{xx}(\mathbf{Q},\omega)$ in Fig. 2(d).

IV. SPIN SUSCEPTIBILITY OF THE SPIN-VALLEY HALF-METALLIC PHASE

According to Eq. (16), in the SVHM state both $\langle S_x(\mathbf{r})\rangle$ and $\langle S_y(\mathbf{r})\rangle$ are nonzero. Therefore, the rotational symmetry around the x axis is broken, and all diagonal components of the susceptibility tensor may differ from each other. As for off-diagonal components, they remain zero. This is a consequence of the electron-hole symmetry of the bands (1). If the electron and hole valleys are asymmetrical, the off-diagonal elements acquire finite values. Specifically, we calculate separately all diagonal components of the susceptibility tensor, assuming $m_a=m_b$ in band structure (1). Then we introduce an asymmetry between the electron and hole bands (1) through the difference in effective masses $m_a\neq m_b$ and estimate components $\tilde{\chi}_{xy}(\mathbf{Q},\omega)$ and $\tilde{\chi}_{yx}(\mathbf{Q},\omega)$.

For numerical calculations we take the doping value, defined in Eq. (24). We obtain the order parameter $\Delta_\sigma=0.5\Delta_0$ from Eq. (11) and the chemical potential $\mu=0.625\Delta_0$ using Eq. (11) of Ref. [3].

A. Diagonal components of the susceptibility tensor

The dependence of the diagonal components on frequency ω is presented in Fig. 3. As we already mentioned in Sec. III A, within our model, the tensor components are insensitive to the direction of $\mathbf{q}$, only the absolute value of the transferred momentum q matters. To illustrate the dependence

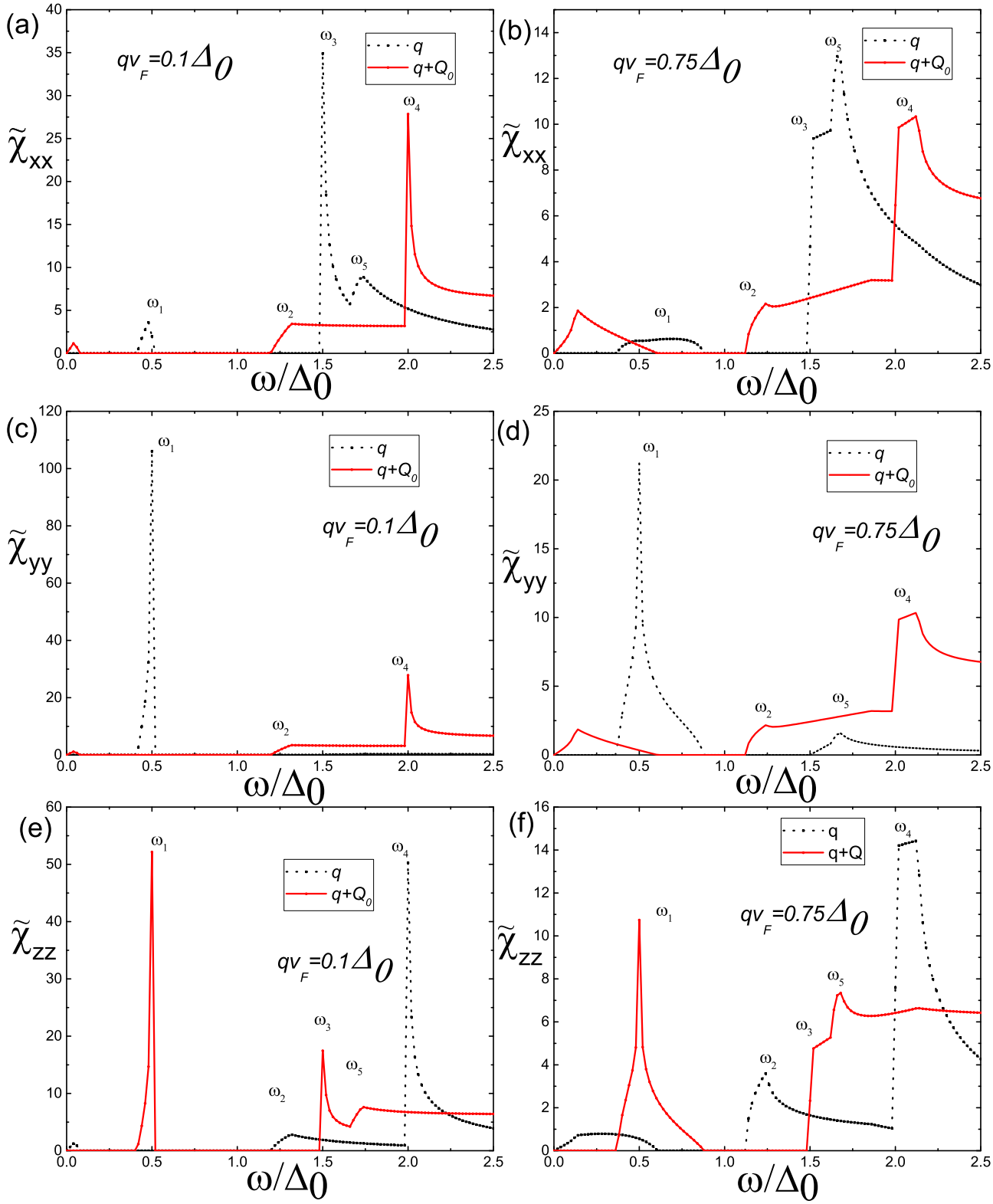

FIG. 3. The diagonal components of the susceptibility tensor $\tilde{\chi}^{s,f}(\mathbf{Q},\omega)$ at fixed momentum $\mathbf{Q}$ versus frequency ω in the SVHM phase. Dot curves show the slow part of the susceptibility calculated for $\mathbf{Q}=\mathbf{q}$; solid curves show the fast part of the susceptibility calculated for $\mathbf{Q}=\mathbf{q}\pm\mathbf{Q}_0$. Panels (a) and (b) present $\tilde{\chi}_{xx}(\mathbf{Q},\omega)$, panels (c) and (d) present $\tilde{\chi}_{yy}(\mathbf{Q},\omega)$, and panels (e) and (f) present $\tilde{\chi}_{zz}(\mathbf{Q},\omega)$ correspondingly. The data in panels (a), (c), and (e) is plotted for $q=0.1\Delta_0/v_F$. The data in panels (b), (d), and (f) is plotted for $q=0.75\Delta_0/v_F$. The (weak) peaks at the lowest frequency are due to intraband transitions within the conduction band. All other peaks are caused by transitions between bands. These transitions are marked by arrows in the inset of Fig. 1(d). Each threshold frequency $\omega_1,\ldots,\omega_5$ represents the opening of a new interband scattering channel. They are determined by Eq. (32).

on q, the curves in panels 3(a), 3(c) and 3(e) are plotted for $q = 0.1\Delta_0/v_F$; the other three panels show the diagonal components at $q = 0.75\Delta_0/v_F$.

The peaks that start from zero frequency are due to the intraband scattering processes. They are similar to the low-energy peaks discussed in Sec. III in the context of the SDW.

In Fig. 3, finite-frequency spectral features (peaks or steps), marked by $\omega_1, \ldots, \omega_5$, arise due to the interband electron transitions. These transitions are illustrated in the inset in Fig. 1(d). Frequencies ω_n may be found in the same manner as $\omega_2^{\rm sdw}$. One needs to find minimum frequency at which a solution of the equation

$$\omega_n = E_f - E_i \tag{31}$$

still exists. In Eq. (31) E_f and E_i are final and initial energies of the excited electron. State at E_f must be empty and state at E_i must be occupied in the ground state to allow excitation process. For five excitations channels shown in Fig. 3, we derive five threshold frequencies. For doping level given by Eq. (24) these frequencies are

$$\begin{aligned}
\omega_1 &= \sqrt{\max\left(\sqrt{\mu^2-\Delta_\sigma^2} - v_F q, 0\right)^2 + \Delta_0^2} - \mu,\\
\omega_2 &= \mu + \sqrt{\max\left(\sqrt{\mu^2-\Delta_\sigma^2} - v_F q, 0\right)^2 + \Delta_\sigma^2},\\
\omega_3 &= \Delta_0 + \Delta_\sigma,\\
\omega_4 &= 2\Delta_0,\\
\omega_5 &= \mu + \sqrt{\max\left(\sqrt{\mu^2-\Delta_\sigma^2} - v_F q, 0\right)^2 + \Delta_0^2}.
\end{aligned} \tag{32}$$

Numerical value of the above frequencies is in the perfect agreement with the threshold frequencies in Fig. 3. As a result of a more complex band structure, the SVHM neutron scattering spectrum has richer structure than the spectrum of the SDW. In Figs. 3(a), 3(c) and 3(e), which represent the spectra for $q = 0.1\Delta_0/v_{\rm F}$, one can discern three spectral peaks (at ω_1, ω_3, and ω_4) and two steplike features (at ω_2 and ω_5). The intensities of these spectral components demonstrate nontrivial dependence on spin polarization. At higher q, the peaks broaden and merge. However, the characteristic frequencies remain discernible even in such a regime.

B. Off-diagonal components of the susceptibility tensor

Besides the structure of the diagonal components of the susceptibility tensor, the SVHM has yet another distinction that separates it from the SDW. As we already pointed out above, the SVHM phase may have finite values of the off-diagonal components $\tilde{\chi}_{xy}$ and $\tilde{\chi}_{yx}$ when the perfect electron-hole symmetry is broken. (For the SDW, these components vanish due to the rotation symmetry).

To study the off-diagonal components, we break the electron-hole symmetry in our model by introducing the difference between the effective masses of electrons and holes

$$\frac{m_b - m_a}{m_b + m_a} = 0.1. \tag{33}$$

In such a regime, we evaluate the off-diagonal components numerically.

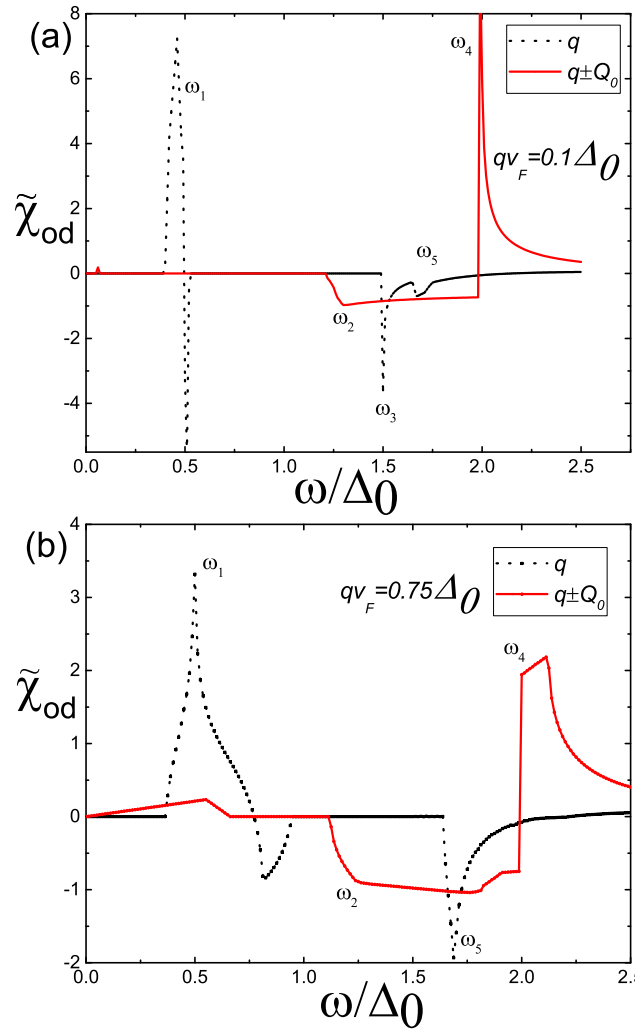

FIG. 4. The off-diagonal component of the susceptibility tensor $\tilde{\chi}_{xy}^{\rm s,f}(\mathbf{Q},\omega)$ at fixed momentum $\mathbf{Q}$ versus frequency ω in the SVHM phase. Dot curves show the slow part of the susceptibility calculated for $\mathbf{Q} = \mathbf{q}$; solid curves show the fast part of the susceptibility calculated for $\mathbf{Q} = \mathbf{q} \pm \mathbf{Q}_0$. The data in panel (a) is plotted for $q = 0.1\Delta_0/v_F$. The data in panel (b) is plotted for $q = 0.75\Delta_0/v_F$. Each threshold frequency $\omega_1, \ldots, \omega_5$ represents the opening of a new interband scattering channel. They are determined by Eq. (32).

Figure 4 shows the dependence $\tilde{\chi}_{xy}$ on frequency ω. Panel 4(a) is plotted for $q = 0.1\Delta_0/v_F$, and panel 4(b) is plotted for $q = 0.75\Delta_0/v_F$. As for $\tilde{\chi}_{yx}$, it can be determined using the relation:

$$\tilde{\chi}_{xy}(\mathbf{Q},\omega) = -\tilde{\chi}_{yx}(\mathbf{Q},\omega). \tag{34}$$

This equality can be derived by substitution of Eq. (18) into Eq. (20), and it follows from the anticommutation rule for Pauli matrices $\sigma_x\sigma_y = -\sigma_y\sigma_x$. Note also that, unlike $\tilde{\chi}_{\alpha\alpha}^{\rm s,f}$, which cannot be negative, the off-diagonal components of the tensor are not constrained by such a requirement, and $\tilde{\chi}_{xy}^{\rm s,f}$ can be of either sign, as indeed seen in Fig. 4.

The same five scattering channels depicted in the inset of Fig. 1(d) control the structure of the off-diagonal components. We see peaks at frequencies ω_1, ω_3, ω_4, and ω_5, as well as

a steplike feature at ω_2. The intensities of the peaks at ω_3 and ω_5 are particularly sensitive to q in the chosen range of parameters. One can also notice that the peak at ω_1 acquires 'a shadow' peak with the opposite sign at somewhat higher ω.

V. DISCUSSION AND CONCLUSIONS

Our study is motivated by the question if the neutron scattering can be used to distinguish the SDW and the SVHM phases. With this aim in mind, we calculated the dynamical spin susceptibility tensor of both phases as a function of frequency at fixed momentum. It is demonstrated that the susceptibilities of the SDW and SVHM have two well-noticeable qualitative distinctions.

The first appreciable difference is a number of high peaks in the diagonal components of the tensor. The SDW phase has only one large peak. At the same time the SVHM has three high and two weaker and broader features. Since each peak represents an interband transition of electrons, the distinction in the number of peaks can be traced to the number of quasiparticle bands in these phases: four bands in the SVHM phase versus only two bands in the SDW phase.

The second difference occurs if electron-hole symmetry is broken (we model such an asymmetry by introducing nonidentical effective masses of electrons and holes). In this case, the SVHM has finite off-diagonal components of the susceptibility tensor. In the SDW phase these components remain zero (in the SDW phase this property is robust since it is protected by the rotation symmetry around order parameter polarization axis).

The intensity of a specific peak depends on the joint density of states and on a corresponding matrix element. Obviously, both these quantities are functions of ω and q. In addition, matrix elements depend also on axis labels [for example, the matrix element for χ_{yy} is not necessary equal to the matrix element for χ_{zz}]. Consequently, the intensity of a peak representing a specific inelastic scattering channel is sensitive to polarization. For example, the peak at $\omega = \omega_1$ in χ^{s}_{xx} is much weaker than the same peak in χ^{s}_{yy}, see Figs. 3(a) and 3(c). As for χ^{s}_{zz}, it demonstrates no peak at $\omega = \omega_1$, see Fig. 3(e).

In our model, the joint density of states (30) diverges when the Pauli principle allows for transition between the edges of the bands. This is the case for the transitions at $\omega = \omega_{1,3,4}$. If the large joint density of states is accompanied by a finite matrix element, the peak intensity is particularly strong. For example, matrix elements at ω_1 and ω_4 in Fig. 3(e) are large, while the matrix element at ω_3 in the same panel is low.

Our calculations were performed for commensurate homogeneous phases only. However, we expect that qualitative behavior of the dynamical spin susceptibility survives in the incommensurate phases as well. Indeed, the most pronounced qualitative differences between the spectra of the commensurate phases are associated either with equality (22) or with the fact that the SDW state has two single-electron bands while the SVHM state hosts four such bands. Both these properties survive in the incommensurate phases. Specifically, the relation (22) is a consequence of the uniaxial spin-rotation invariance of the SDW phase, which holds regardless of the commensurability of the order parameter. As for the band structure of the incommensurate SVHM phase, the expressions for its four bands were derived in Ref. [9], see Eq. (56) there. Thus, we expect that the inelastic neutron scattering can be used to detect the SVHM state even for the incommensurate order parameter.

Naturally, the model used in this paper is insufficient to describe the properties of a specific system quantitatively. Rather, the presented analysis is the first necessary step toward possible identification of the SVHM phase in real materials. The elementary Hamiltonian discussed above should be considered as a minimal model sufficiently complex as to retain the studied phenomena, yet simple enough to allow for semianalytical treatment.

Our model neglects numerous details, like disorder, nesting imperfections, non-SDW electronic bands, which complicate the theoretical study of a real material. Although a thorough research into these issues is required, some preliminary arguments can be formulated even at this stage. For example, imperfect nesting was briefly discussed in Refs. [3,9]. It was concluded that the SVHM state remains stable even in the presence of the imperfect nesting. As for the neutron spectrum, nesting imperfections, as well as other band structure features unaccounted for by our simple model, likely affect quantitative properties of the spectrum (for example, the peaks intensities). However, the total number of interband transitions in the SVHM phase is a consequence of the SVHM-specific violation of the symmetry between the sectors. This violation is insensitive to the underlying band structure. Thus, we expect the qualitative stability of the neutron spectrum relative to a wide class of modifications of the single-electron bands.

Another ever-present factor influencing electronic properties of a condensed matter system is disorder. In a sample with chemical doping, disorder is virtually unavoidable: Dopant atoms introduce randomly placed irregularities to the host lattice. While in some cases the disorder may cause drastic modifications to material's properties (for example, localize electronic wave functions), in other situations its effects are perturbatively weak [51]. To stabilize our SVHM phase, the dopant atoms concentration does not have to be large. Indeed, one can notice analyzing Eq. (15) that characteristic doping level in the theory of the SVHM is $x_0 = N_F \Delta_0$. Within the weak-coupling framework, this scale is small since Δ_0 is much smaller than the characteristic single-electron energies, like the bandwidth. Consequently, we expect relatively mild disorder effects.

Let us finally discuss the candidate materials classes. We hypothesize that several families of materials can host the SVHM phase: chromium and its alloys [30–33], some topological insulators [34], iron-based materials [35], as well as other systems [36–38]. Consider, for example, $CoCr_2O_4$. Recent *ab initio* study demonstrates [52] that $CoCr_2O_4$ has a multisheet Fermi surface with nesting, unstable with respect to spin ordering. Doping with iron atoms drives the material toward a half-metallic state. Our previous results [3,9] allow us to speculate that in such a situation the energies of the SVHM and the usual half-metallic state can be close to each other. Yet, since the spin-valley polarization of the Fermi surface is not evaluated in a typical first-principle study, should the SVHM state become a ground state of the studied system, such a situation may pass completely undetected.

Another family of materials worth considering for the SVHM phase is the Bechgaard salts [53,54]. It is believed that in this class of materials the SDW instability is triggered by nesting of the Fermi surface [55]. In experiment, the nesting quality in the Bechgaard salts is weakened by the external pressure. It is conceivable that, as a response to the pressure-induced nesting deterioration, redistribution of the electrons between different sectors may start to improve the nesting in at least one sector. As we explained in Sec. II A, the uneven distribution of the electrons between the sectors implies the spin-valley polarization of the Fermi surface and the SVHM state.

In conclusion, we calculated the dynamical spin susceptibility for the doped spin-density wave state and the doped spin-valley half-metallic state at different momenta. Due to more complex band structure, the SVHM spin susceptibility tensor demonstrates richer frequency dependence and may have finite off-diagonal components. Our analysis shows that the inelastic neutron scattering may be used to distinguish the SDW and the SVHM phases in experiment.

ACKNOWLEDGMENTS

This work was partially supported by the JSPS-Russian Foundation for Basic Research joint Project No. 19-52-50015. One of us (D.A.K.) was partially supported by the Foundation for the Advancement of Theoretical Physics and Mathematics "BASIS."

[1] T. M. Rice, Band-structure effects in itinerant antiferromagnetism, Phys. Rev. B **2**, 3619 (1970).
[2] A. L. Rakhmanov, A. V. Rozhkov, A. O. Sboychakov, and F. Nori, Phase separation of antiferromagnetic ground states in systems with imperfect nesting, Phys. Rev. B **87**, 075128 (2013).
[3] A. V. Rozhkov, A. L. Rakhmanov, A. O. Sboychakov, K. I. Kugel, and F. Nori, Spin-Valley Half-Metal as a Prospective Material for Spin Valleytronics, Phys. Rev. Lett. **119**, 107601 (2017).
[4] Y.-D. Chuang, A. D. Gromko, D. S. Dessau, T. Kimura, and Y. Tokura, Fermi surface nesting and nanoscale fluctuating charge/orbital ordering in colossal magnetoresistive oxides, Science **292**, 1509 (2001).
[5] M. L. Kiesel, C. Platt, W. Hanke, D. A. Abanin, and R. Thomale, Competing many-body instabilities and unconventional superconductivity in graphene, Phys. Rev. B **86**, 020507 (2012).
[6] L. P. Gor'kov and G. B. Teitel'baum, Spatial inhomogeneities in iron pnictide superconductors: The formation of charge stripes, Phys. Rev. B **82**, 020510 (2010).
[7] F. Šimkovic, X.-W. Liu, Y. Deng, and E. Kozik, Ground-state phase diagram of the repulsive fermionic $t - t'$ Hubbard model on the square lattice from weak coupling, Phys. Rev. B **94**, 085106 (2016).
[8] K. S. Mosoyan, A. V. Rozhkov, A. O. Sboychakov, and A. L. Rakhmanov, Spin-density wave state in simple hexagonal graphite, Phys. Rev. B **97**, 075131 (2018).
[9] A. L. Rakhmanov, A. O. Sboychakov, K. I. Kugel, A. V. Rozhkov, and F. Nori, Spin-valley half-metal in systems with Fermi surface nesting, Phys. Rev. B **98**, 155141 (2018).
[10] R. S. Akzyanov and A. V. Rozhkov, Generation of localized magnetic moments in the charge-density-wave state, Eur. Phys. J. B **88**, 196 (2015).
[11] R. Nandkishore, G.-W. Chern, and A. V. Chubukov, Itinerant Half-Metal Spin-Density-Wave State on the Hexagonal Lattice, Phys. Rev. Lett. **108**, 227204 (2012).
[12] A. O. Sboychakov, A. L. Rakhmanov, K. I. Kugel, A. V. Rozhkov, and F. Nori, Magnetic field effects in electron systems with imperfect nesting, Phys. Rev. B **95**, 014203 (2017).
[13] J. González and T. Stauber, Kohn-Luttinger Superconductivity in Twisted Bilayer Graphene, Phys. Rev. Lett. **122**, 026801 (2019).
[14] A. O. Sboychakov, A. V. Rozhkov, A. L. Rakhmanov, and F. Nori, Externally Controlled Magnetism and Band Gap in Twisted Bilayer Graphene, Phys. Rev. Lett. **120**, 266402 (2018).
[15] A. L. Rakhmanov, K. I. Kugel, M. Y. Kagan, A. V. Rozhkov, and A. O. Sboychakov, Inhomogeneous electron states in the systems with imperfect nesting, JETP Lett. **105**, 806 (2017).
[16] R. S. Akzyanov, A. O. Sboychakov, A. V. Rozhkov, A. L. Rakhmanov, and F. Nori, AA-stacked bilayer graphene in an applied electric field: Tunable antiferromagnetism and coexisting exciton order parameter, Phys. Rev. B **90**, 155415 (2014).
[17] A. O. Sboychakov, A. L. Rakhmanov, A. V. Rozhkov, and F. Nori, Metal-insulator transition and phase separation in doped AA-stacked graphene bilayer, Phys. Rev. B **87**, 121401 (2013).
[18] A. O. Sboychakov, A. V. Rozhkov, K. I. Kugel, A. L. Rakhmanov, and F. Nori, Electronic phase separation in iron pnictides, Phys. Rev. B **88**, 195142 (2013).
[19] A. V. Rozhkov, Superconductivity without attraction in a quasi-one-dimensional metal, Phys. Rev. B **79**, 224520 (2009).
[20] A. V. Rozhkov, Competition between different order parameters in a quasi-one-dimensional superconductor, Phys. Rev. B **79**, 224501 (2009).
[21] A. V. Rozhkov, Variational description of the dimensional crossover in an array of coupled one-dimensional conductors, Phys. Rev. B **68**, 115108 (2003).
[22] P. Hirschfeld, M. Korshunov, and I. Mazin, Gap symmetry and structure of Fe-based superconductors, Rep. Prog. Phys. **74**, 124508 (2011).
[23] R. M. Fernandes and J. Schmalian, Competing order and nature of the pairing state in the iron pnictides, Phys. Rev. B **82**, 014521 (2010).
[24] G. Grüner, *Density Waves In Solids* (Addison-Wesley Publishing Company, Reading, Massachusetts, 1994).
[25] M. D. Johannes and I. I. Mazin, Fermi surface nesting and the origin of charge density waves in metals, Phys. Rev. B **77**, 165135 (2008).
[26] R. A. de Groot, F. M. Mueller, P. G. van Engen, and K. H. J. Buschow, New Class of Materials: Half-Metallic Ferromagnets, Phys. Rev. Lett. **50**, 2024 (1983).
[27] M. I. Katsnelson, V. Y. Irkhin, L. Chioncel, A. I. Lichtenstein, and R. A. de Groot, Half-metallic ferromagnets: From band structure to many-body effects, Rev. Mod. Phys. **80**, 315 (2008).
[28] M. Eschrig, Spin-polarized supercurrents for spintronics: A review of current progress, Rep. Prog. Phys. **78**, 104501 (2015).

[29] D. Zhong, K. L. Seyler, X. Linpeng, R. Cheng, N. Sivadas, B. Huang, E. Schmidgall, T. Taniguchi, K. Watanabe, M. A. McGuire *et al.*, Van der Waals engineering of ferromagnetic semiconductor heterostructures for spin and valleytronics, Sci. Adv. **3**, e1603113 (2017).

[30] E. Fawcett, Spin-density-wave antiferromagnetism in chromium, Rev. Mod. Phys. **60**, 209 (1988).

[31] X. Sun, W. Li, X. Wang, Q. Sui, T. Zhang, Z. Wang, L. Liu, D. Li, S. Feng, S. Zhong *et al.*, Room temperature 2D ferromagnetism in few-layered 1T-CrTe _2, arXiv:1909.09797.

[32] D. A. Sokolov, M. C. Aronson, L. Wu, Y. Zhu, C. Nelson, J. F. Mansfield, K. Sun, R. Erwin, J. W. Lynn, M. Lumsden *et al.*, Neutron, electron, and x-ray scattering investigation of $Cr_{1-x}V_x$ near quantum criticality, Phys. Rev. B **90**, 035139 (2014).

[33] K. Fukamichi, Basic and Applied Research of Transition-metal Based Magnetic Materials, J. Magn. Soc. Jpn. **41**, 81 (2017).

[34] J.-H. Jiang and S. Wu, Spin susceptibility and helical magnetic order at the edges/surfaces of topological insulators due to Fermi surface nesting, Phys. Rev. B **83**, 205124 (2011).

[35] P. Dai, J. Hu, and E. Dagotto, Magnetism and its microscopic origin in iron-based high-temperature superconductors, Nat. Phys. **8**, 709 (2012).

[36] Y. Feng, J. Wang, D. M. Silevitch, B. Mihaila, J. W. Kim, J.-Q. Yan, R. K. Schulze, N. Woo, A. Palmer, Y. Ren *et al.*, Incommensurate antiferromagnetism in a pure spin system via cooperative organization of local and itinerant moments, Proc. Nat. Acad. Sci. **110**, 3287 (2013).

[37] R. Jaramillo, Y. Feng, and T. F. Rosenbaum, Diffraction lineshapes, Fermi surface nesting, and quantum criticality in antiferromagnetic chromium at high pressure (invited), J. Appl. Phys. **107**, 09E116 (2010).

[38] J. E. Ortmann, J. Y. Liu, J. Hu, M. Zhu, J. Peng, M. Matsuda, X. Ke, and Z. Q. Mao, Competition Between Antiferromagnetism and Ferromagnetism in Sr_2RuO_4 Probed by Mn and Co Doping, Sci. Rep. **3**, 2950 (2013).

[39] M. M. Korshunov and I. Eremin, Theory of magnetic excitations in iron-based layered superconductors, Phys. Rev. B **78**, 140509 (2008).

[40] R. Nandkishore, L. S. Levitov, and A. V. Chubukov, Chiral superconductivity from repulsive interactions in doped graphene, Nat. Phys. **8**, 158 (2012).

[41] B. V. Fine, Magnetic vortices instead of stripes: Another interpretation of magnetic neutron scattering in lanthanum cuprates, Phys. Rev. B **75**, 060504 (2007).

[42] T. Egami, B. Fine, D. Parshall, A. Subedi, and D. Singh, Spin-lattice coupling and superconductivity in Fe pnictides, Adv. Condens. Matter Phys. **2010**, 164916 (2010).

[43] T. Egami, B. Fine, D. Singh, D. Parshall, C. de la Cruz, and P. Dai, Spin-lattice coupling in iron-pnictide superconductors, Physica C: Superconductivity and its Applications **470**, S294 (2010).

[44] O. Lychkovskiy and B. V. Fine, Spin excitation spectrum of high-temperature cuprate superconductors from finite cluster simulations, J. Phys.: Condens. Matter **30**, 405801 (2018).

[45] Y. S. Lee, R. J. Birgeneau, M. A. Kastner, Y. Endoh, S. Wakimoto, K. Yamada, R. W. Erwin, S.-H. Lee, and G. Shirane, Neutron-scattering study of spin-density wave order in the superconducting state of excess-oxygen-doped La_2CuO_{4+y}, Phys. Rev. B **60**, 3643 (1999).

[46] Y. Qiu, M. Kofu, W. Bao, S.-H. Lee, Q. Huang, T. Yildirim, J. R. D. Copley, J. W. Lynn, T. Wu, G. Wu *et al.*, Neutron-scattering study of the oxypnictide superconductor $LaFeAsO_{0.87}F_{0.13}$, Phys. Rev. B **78**, 052508 (2008).

[47] I. I. Mazin and V. M. Yakovenko, Neutron Scattering and Superconducting Order Parameter in $YBa_2Cu_3O_7$, Phys. Rev. Lett. **75**, 4134 (1995).

[48] N. Qureshi, P. Steffens, Y. Drees, A. C. Komarek, D. Lamago, Y. Sidis, L. Harnagea, H.-J. Grafe, S. Wurmehl, B. Büchner *et al.*, Inelastic Neutron-Scattering Measurements of Incommensurate Magnetic Excitations on Superconducting LiFeAs Single Crystals, Phys. Rev. Lett. **108**, 117001 (2012).

[49] G. D. Mahan, *Many Particle Physics, Third Edition* (Plenum, New York, 2000).

[50] A. Furrer, J. Mesot, and T. Strässle, *Neutron scattering in condensed matter physics* (World Scientific Publishing Company, Singapore, 2009).

[51] S. V. Kokanova and A. V. Rozhkov, Disorder correction to the Néel temperature of ruthenium-doped $BaFe_2As_2$: Theoretical analysis, Phys. Rev. B **99**, 075134 (2019).

[52] S. Ganguly, R. Chimata, and B. Sanyal, Overcoming magnetic frustration and promoting half-metallicity in spinel $CoCr_2O_4$ by doping with Fe, Phys. Rev. B **92**, 224417 (2015).

[53] A. Lebed, ed., *The physics of organic superconductors and conductors* (Springer, 2008).

[54] T. Ishiguro, K. Yamaji, and G. Saito, *Organic Superconductors* (Springer, Heidelberg, 1998).

[55] A. L. Rakhmanov, K. Kugel, and A. O. Sboychakov, Coexistence of Spin Density Wave and Metallic Phases Under Pressure, J. Supercond. Nov. Magn. (2020).